Submitted to Phys. Chem. Chem. Phys, 3/31/2020
Revised 5/19/2020

On the Nonadiabatic Collisional Quenching of OH(A) by H_2: A Four Coupled Quasi-Diabatic State Description

Christopher L. Malbon[a,*] Bin Zhao[b,#], Hua Guo[b] and David R. Yarkony[a]

[a]*Department of Chemistry, Johns Hopkins University, Baltimore, MD 21218, USA*
[b]*Department of Chemistry and Chemical Biology, University of New Mexico, Albuquerque, NM, 87131, USA*
[#]*Present address: Theoretische Chemie, Fakultät für Chemie, Universität Bielefeld, Universitätsstr. 25, D-33615 Bielefeld, Germany*

Abstract

A four-state diabatic potential energy matrix (DPEM), $\mathbf{H}^d$, for the description of the nonadiabatic quenching of OH($A\,^2\Sigma^+$) by collisions with H_2 is reported. The DPEM is constructed as a fit to adiabatic energies, energy gradients, and derivative couplings obtained exclusively from multireference configuration interaction wave functions. A four-adiabatic-electronic-state representation is used in order to describe all energetically accessible regions of the nuclear coordinate space. Partial permutation-inversion symmetry is incorporated into the representation. The fit is based on electronic structure data at 42882 points, described by over 1.6 million least squares equations with a root mean square (mean unsigned) error of 178 (83) cm^{-1}. Comparison of *ab initio* and $\mathbf{H}^d$ determined minima, saddle points, and energy minimized points on C_{2v}, $C_{s,}$ $C_{\infty v}$, and C_1 (noncoplanar) portions of two conical intersection seams are used to establish the accuracy of the $\mathbf{H}^d$.

I. Introduction

The central role of hydrogen abstraction by the hydroxyl radical in combustion environments[1] (a chain propagation step in the ignition of hydrocarbons) and atmospheric environments[2-3] (the oxidation of trace gases) is well established, making the concentration of the hydroxyl radical an important measure of reaction kinetics in atmospheric and combustion chemistry. Laser induced fluorescence (LIF) based on the well-characterized $A^2\Sigma^+$-$X^2\Pi$ band is most often used for such analysis; however, collisional quenching of the target molecule, in this case $OH(A^2\Sigma^+)$, by collisional partners reduces the accuracy of LIF measurements.[1] To determine the ground-state population, an understanding of these nonradiative quenching processes is required.

The collisional quenching of $OH(A^2\Sigma^+)$ by molecular hydrogen has become an archetypical system for studying nonadiabatic quenching. The reaction proceeds via one of two pathways: nonreactive quenching

$$OH(A^2\Sigma^+) + H_2 \rightarrow OH(X^2\Pi) + H_2 \quad (1a)$$

or reactive quenching

$$OH(A^2\Sigma^+) + H_2 \rightarrow H_2O(\tilde{X}^1A_1) + H \quad (1b)$$

where seams of conical intersections facilitate nonadiabatic transitions from $OH(A^2\Sigma^+) + H_2$ to the ground electronic state.[4-5] LIF experiments by Lester and coworkers, probing the OH $A - X$ transition of the products, have shown (1b) is the favored pathway, accounting for >80% of quenching events.[6-7] Additionally, Doppler spectroscopy of H atom products, also by the Lester laboratory, showed two channels for (1b): hydrogen abstraction and insertion.[8-9] Experiments colliding deuterated hydroxyl and molecular hydrogen found the abstraction pathway favored by a 3:1 ratio.[10] Crossed molecular beam experiments by Davis et al., colliding hydroxyl and molecular deuterium at higher collision energies, showed direct hydrogen abstraction is the dominant reactive pathway.[11] Lester, Alexander and coworkers provided a combined experimental/computational study of the nonreactive quenching channel, including the spin-orbit splitting and the Λ-doublet propensity in $OH(X^2\Pi_\Omega)$ Ω=3/2,1/2.[12] The small spin-orbit

coupling in $OH(X^2\Pi_\Omega)$ which is quenched in the H_2O product channel is not included in this work.

Significant theoretical work has been applied towards the understanding and reproduction of the aforementioned experimental results. Yarkony and coworkers mapped the seams of same-symmetry conical intersections responsible for nonadiabatic transitions involving the (1a) and (1b) pathways.[4-5] Gradient-directed paths started at these crossings indicated that dynamics would favor nonreactive quenching. Classical trajectory simulations on the ground state potential energy surface (PES) by Bowman et al. starting from the conical intersections reported by Yarkony and Hoffman found a reactive to non-reactive quenching ratio of 2.3:1[13] or 70:30.[14] Han and coworkers performed quantum scattering calculations on PESs for the A' ground and first excited states and reported branching ratios for reactive and nonreactive quenching of 5:1 at a collision energy of 0.06 eV and 3:1 at a collision energy of 0.4 eV.[15] The omission of the A'' state, and in the case of Han's study the exclusion of out-of-plane motion, may have had a significant effect on these results.

Zhang and coworkers presented coupled PESs for the three lowest states of $OH + H_2$ using a quasi-diabatic potential energy matrix (DPEM)[16] based on modified Shepard interpolation.[17] Surface hopping classical trajectories began on the $OH(A^2\Sigma^+) + H_2$ state, however, showed the dominant product channel to be (1a). A detailed presentation of the seams of conical intersection coupling the 1^2A and 2^2A states and $2^2A$and 3^2A states of $OH+H_2$ was reported by Dillon and Yarkony.[18] They showed that a significant non-planar portion of the 2^2A - 3^2A seam is below the $OH(A^2\Sigma^+) + H_2$ state asymptote, providing energy-accessible pathways for nonadiabatic transitions. Such out-of-plane intersections had been omitted from all previous studies. A second study by Dillon and Yarkony, using linear-synchronous transit (LST) paths, posited that an out-of-plane, complex-forming, pathway for insertion was a main channel for reactive quenching.[19] This pathway would be absent from previous dynamics studies, and, if it were a significant contributor to $H_2O + H$ products, it would help resolve the discrepancies

between theoretical and experimental results; however, the want of full-dimensional nonadiabatic dynamics precludes certainty.

Full-dimensional quantum dynamics requires global PESs that are accurate in all energy-accessible and chemically relevant regions of the nuclear coordinate space.[20-21] It is essential that the PESs reliably describe the energies, gradients, and nonadiabatic couplings; as well as minima, saddle points, and seams of conical intersections. Recently, Truhlar and coworkers have reported a three-state diabatic representation of the 1, 2, 3^2A states.[22] In addition to the obvious difference of 3 versus 4 diabatic states, which will be addressed in Section II, this report differs in the electronic structure method used and the diabatization and fitting procedure employed. Thus, there is much to be learned from the comparison of these two coupled-state representations and the ensuing nonadiabatic dynamics. This will be the subject of future work.

A robust fitting-while-diabatizing procedure[23] previously applied to ammonia,[24-25] phenol,[23, 26] and hydroxymethyl[27] is employed here to construct a DPEM describing the collision of the hydroxyl radical and molecular hydrogen. The global, four-state, coupled diabatic representation, the 1, 2, 3, 4 ^{2}A states $\mathbf{H}^d$, reported here is built from high-level, multi-reference *ab initio* data in all relevant regions of the nuclear coordinate space. The representation will enable full-dimensional dynamics simulations at an accuracy not attainable via on-the-fly methods. Section II of this work describes the *ab initio* electronic structure treatment. It also outlines the challenges in describing the $OH + H_2$ system. Section III provides an overview of the representation, $\mathbf{H}^d$. Section IV discusses the accuracy of $\mathbf{H}^d$, and explains how well it reproduces the underlying *ab initio* data, previous theoretical results, and experimental results where possible. Section IV summarizes and discusses future directions.

II. Electronic Structure

The description of the bimolecular collision of OH with H_2 requires a flexible, multi-reference electronic structure treatment of the system wavefunctions. To construct the multi-reference single and double excitation configuration interaction (MR-SDCI) expansion, the reference space at and reaction paths from high symmetry (D_{3h} and C_{3v}) OH_3 geometries are

considered. The oxygen $1s$ orbital is doubly-occupied throughout the nuclear coordinate space. The ground electronic state configuration is (excluding the oxygen $1s$ orbital) three doubly-occupied OH σ bonding orbitals, σ_{OH}, one doubly-occupied nonbonding oxygen lone pair ($2p_z$) orbital, n_{O}, and one singly-occupied Rydberg orbital $3s$. The first, second, and third excited states are excitations from the $3s$ orbital into $3p_x$, $3p_y$, and $3p_z$ orbitals, respectively. Continuing, as any OH bond may be broken, all three σ^*_{OH} orbitals must be included. It is required then that the MR-SDCI reference space includes eleven orbitals and nine electrons. In this work, an additional orbital is added for increased flexibility. The three reactant OH states, $\mathrm{X}^2\Pi(\ldots 4\sigma^2 1\pi^3)$ and $\mathrm{A}^2\Sigma^+(\ldots 4\sigma 1\pi^4)$, at the OH+$H_2$ asymptote are well described by this reference space. The question then arises whether to truncate the reference space at the three states as suggested by the reactant channel or add another orbital/state to the reference space. The choice of four states was made on the basis of the work by Dillon and Yarkony (DY1),[19] which showed that in the above noted high symmetry region the $3p_z$ Rydberg state is 7388 cm^{-1} (9179 cm^{-1} in this work) below the $\mathrm{OH}(\mathrm{A}^2\Sigma^+) + \mathrm{H}_2$ asymptote. The consequences of this decision are discussed below.

A restricted active-space (RAS) scheme is employed to reduce the computational cost. Two active spaces are defined (parentheses indicate the result of allowed excitations): a four-orbital, eight (seven)-electron space; and an eight orbital, one (two) electron space. The orbitals are constructed from cc-pVTZ bases, with $3s$ ($\xi = 0.032$) and $3p$ ($\xi = 0.028$) orbitals added to oxygen, and are optimized within the reference space by a five-state averaged (equal weights) multiconfiguration self-consistent field (SA-MCSCF) procedure. From this reference space, single and double excitations into virtual orbitals build the MR-SDCI wavefunction of 6 846 859 configuration state functions (CSFs). Despite its small size, the expansion is flexible and robust, and describes well all regions of the relevant OH + H_2 configuration space.

Unless otherwise noted all electronic energies are given in cm^{-1} relative to the reactant $H_2(^1\Sigma_g^+)$ and $\mathrm{OH}(\mathrm{A}^2\Sigma^+)$ at their equilibrium geometries. All electronic structure calculations employed the COLUMBUS suite of electronic structure codes.[28]

III. Form of $\mathbf{H}^d$

A. General

Electronic energies $E^{a,J,(m)}(\mathbf{R})$, energy gradients, and derivative couplings are determined from the adiabatic electronic Schrödinger equation

$$[\mathbf{H}^d(\mathbf{R}) - \mathbf{I}E^{(a),J,m}(\mathbf{R})]\mathbf{d}^J(\mathbf{R}) = 0. \quad (2)$$

$\mathbf{H}^d(\mathbf{R})$ the diabatic $N^{state} \times N^{state}$ Hamiltonian (here $N^{state} = 4$), is the key product of this work. It has the form

$$\mathbf{H}^d(\boldsymbol{R}) = \sum_{l=1}^{N^c} V_l[\bar{P}^{\kappa(u(l),v(l))} g(l)]\mathbf{B}^{u(l).v(l)} \quad (3)$$

where $\mathbf{B}^{u,v}$ is an $N^{state} \times N^{state}$ symmetric matrix with the (u,v) and (v,u) elements 1 and the rest 0. The V_l are the N^c linear coefficients determined by the least-squares fitting procedure. $\bar{P}^{\kappa}$ is a group theoretical projection operator for the κth irreducible representation of the complete nuclear permutation-inversion (CNPI) group.[29]

B. Selection of $g^{(l)}(\mathbf{R})$

The monomials, $g^{(l)}(\mathbf{R})$ are constructed as products of elementary stretch, angle, out-of-plane, and dot product functions of the nuclear positions, **R**. See Table SI1 in Supporting Information (SI). The values of their (nonlinear) parameters are given in Table SI2 in SI. The atomic numbering used in Table SI2 and throughout this work is given in Figure 1. The choice of these elementary functions, and the rules for forming the products, $g^{(l)}(\mathbf{R})$ are critical for a proper global fit.

The local regions of a PES can be easily described by quadratic expansions. The challenge in a global fit is fitting the multiple local, quadratic regions with polynomials that may vary from local region to local region in scaling or origin, or both. Increasing the order of the polynomials to third order or fourth order is one solution. However, both increase flexibility at computational cost. The solution is limiting all stretch and angle functions to second order, as it is reasonable to assume these functions can describe any local quadratic region, and introduce "partitioning" functions, $\tanh(x)$ and $\exp[-x^2]$, that are multiplied with the second-order

polynomials to make third-order polynomials capable of describing multiple, separate quadratic regions.

C. CNPI

The CNPI symmetry group allows for a global description of the nuclear geometries. Each diabatic state carries an irreducible representation of the CNPI group for the molecular system. With three equivalent atoms, the CNPI group of the bimolecular collision $OH + H_2$ has twelve symmetry operations. This group is called $\overline{D}_{3h} \equiv S_3 \times I$ (where S_3 is the symmetric group of order 3 and I is the inversion group), since it is isomorphic to the nonabelian point-group of the same name. The two-dimensional irreducible representations of $\overline{D}_{3h}$, denoted E' and E'', complicate the construction of $\mathbf{H}^d$, a consequence of the flexible product form of the monomials, $g^{(l)}$, in $\mathbf{H}^d$. Each $\overline{P}^{\kappa} g^{(l)}$ carries an irreducible representation of the CNPI symmetry group. In the case of nonabelian groups, such as $\overline{D}_{3h}$, distinct linear combinations of the same $g^{(l)}$ carry different irreducible representations. For this reason, an abelian subgroup of $\overline{D}_{3h}$, G_4 (with 2 equivalent atoms and isomorphic to C_{2v}), is used.

A consequence of using the G_4 subgroup operations is that to obtain the full $\overline{D}_{3h}$ symmetry missing permutations must be incorporated "by hand".[30] OH_3 has three equivalent hydrogen atoms, denoted by the triple (a, b, c - see Fig. 1). The standard ordering is defined in this work as (a, b, c) = (1, 2, 3). The S_3 group operations are the identity, e; 3 transpositions, [a,b], [a,c] [b,c]; and two cyclic permutations, [c, a, b] and [b, c, a]. They act on the ordered triple (1, 2, 3) and generate the hydrogen atom permutations: (1, 2, 3), (2, 1, 3), (3, 2, 1), (1, 3, 2) (3, 1, 2), and (2, 3, 1). The G_4 group ($S_2 \times I$) operations treat only hydrogens a and b equivalently and thus generate two permutations, (1, 2, 3) and (2, 1, 3), from the standard ordering. To obtain the four remaining permutations, the *ab initio* geometries and the associated gradients and

couplings are reordered so (a, b, c) = (3, 2, 1) and (a, b, c) = (1, 3, 2). The G_4 group operations generate the remaining permutations, yielding the six permutations of $\overline{D}_{3h}$ required for OH_3. The 6 S_3 permutations are partitioned into three subsets: the standard ordering $\mathcal{S}1$, comprised of (1, 2, 3) and (2, 1, 3); $\mathcal{S}2$ comprised of (3,2,1) and (2,3,1); and $\mathcal{S}3$ comprised of (1, 3, 2) and (3,1,2).

D. Selection of $\mathbf{R}^n$

For clarity, the nuclear coordinate space is divided into five regions following DY1: the entrance channel ($OH+H_2$ structures), the valence region ($HO-H_2$ structures), the linking region (which connects the valence and Rydberg regions and where significant changes in molecular orbital character take place), the Rydberg or exchange region (H_3O structures), and the product channel (HOH+H structures).

The nuclear coordinates, **R**, at which *ab initio* data are computed and then fit are composed of two sets: skeletal data (critical points and linear-synchronous-transit paths between critical points) and trajectory-generated data. The skeletal data builds the initial description of the DPEM, and, as the DPEM is grown from this initial set of data points, the skeletal data set has the largest influence on the final fit. The skeletal data set for $OH + H_2$ has 4035 (1345 unique) points

The trajectory-generated **R** are taken from surface-hopping trajectories[31] based on Tully's fewest switches method[32] with a total electronic energy less than 4000 cm^{-1}. The selected **R,** include the 1^2A and 3^2A van der Waal minima in the entrance channel, 1^2A and 2^2A saddle points in the interaction region, the 1^2A OH_3 minimum in the exchange region, and a "reactive-type" geometry (R(HO-H_2)=2.18 Å, with O facing H_2) in the entrance channel, allowing for the exploration of, and fitting of points from, exclusively energetically relevant regions.

When a trajectory attempts to explore outside the region of the nuclear coordinate space where $\mathbf{H}^d$ reliably reproduces the *ab initio* data (a defined distance from previously fit geometries) the trajectory is halted and several data points along this path are chosen to be added to the fit. This procedure has been outlined in greater detail previously.[23]

E. Sign Issues

There are two classes of sign issues to be dealt with in determining $\mathbf{H}^d$. First at fixed $\mathbf{R}$, the sign of the *ab initio* and $\mathbf{H}^d$ determined derivative couplings must agree. This discrepancy arises from and can be resolved by altering the phases of the eigenvectors of $\mathbf{H}^d$. This sign adjustment must be performed at each geometry and geometric continuity is of no help. The second issue reflects the fact that there does not exist a one-to-one mapping from the matrix elements of $\mathbf{H}^d$ to its spectrum. Changing the sign of one of the diabatic basis states changes the sign of one or more of the elements of $\mathbf{H}^d$ without changing the energies or derivative couplings. This change of basis states would lead to a discontinuous change in the linear coefficients of $\mathbf{H}^d$, but this is precluded by our polynomial representation.

IV. Accuracy of $\mathbf{H}^d$: General Metrics

Table I presents the basic metrics of the fit. The number of data points is the total number after performing the tripling procedure outlined in Section IIIC. As explained in Section IIIC, to describe exchange of three identical particles in the G_4 CNPI group, two additional permutations of the atoms must be generated "by hand." Thus, although the results at symmetry equivalent points should be identical there is fitting error introduced by the least squares procedure. Tables reporting critical point information will also present the results at symmetry equivalent structures. In general, the agreement of the $\mathcal{S}1$, $\mathcal{S}2$, and $\mathcal{S}3$ results in equivalent local region parallels the local accuracy of the fit. Throughout the text, where applicable, results are presented as follows: *ab initio* ($\mathcal{S}1$) [$\mathcal{S}2$, $\mathcal{S}3$] or *ab initio* ($\mathcal{S}1$) when $\mathcal{S}2$, $\mathcal{S}3$ are not reported.

$\mathbf{H}^d$ is constructed from 42882 nuclear geometries, $\mathbf{R}^n$. It is fit to the energies, energy gradients, and derivative couplings at each geometry, subject to a fitting cutoff threshold (E^{cutoff}): states with energies above E^{cutoff} = 5000 cm^{-1} are reduced in weight. The calculated error is reported for energies and gradients below this threshold. Two measures of the fitting error are reported. The root mean square (RMS) error which emphasizes the $\mathbf{R}$ for which the differences between $\mathbf{H}^d$ and the *ab initio* data are large and thus does well describing the fit surfaces' maximal error. The mean-unsigned (MU) error is an evenly-weighted average of all errors, so the

maximal errors are averaged out. Reporting both the RMS and MU errors offers a more complete picture of the quality of the fit representation. The RMS energy error for all states is 177.57 cm^{-1} and the RMS gradient error is 7.29% (See Table I). The MU error for all four states and gradients is 83.49 cm^{-1} and 3.79%, respectively. Table II reports the RMS and MU errors for each state. In Table II, the results from the representation presented here are compared with the results of the representation reported by Truhlar and coworkers.[22]

Figure 2 shows the contribution of data points within an energy range to the accumulating error (RMS and MU errors) for each adiabatic state, and the density of data points at a given energy. The errors, both RMS and MU, for states 1^2A and 2^2A increase gradually up to the E^{cutoff}. The RMS error increases sharply for the 3^2A state between -10000 cm^{-1} and -5000 cm^{-1}; however, the stable MU error and low point density indicate that this increase in RMS error is due to a small number of data points in this energy region. The total RMS error of the 3^2A state decreases beginning at -2000 cm^{-1}. This corresponds to a large spike in the density of 3^2A state data points at 0 cm^{-1}. This is the entrance channel, and $\mathbf{H}^d$ reproduces these data points well. The majority of the 4^2A state data points occur well above E^{cutoff}, but there is a significant density of points below E^{cutoff}, as far down as -9000 cm^{-1}. This is the Rydberg $3p_z$ state in the hydrogen exchange, or Rydberg, region.

V. Accuracy of $\mathbf{H}^d$: Regions of Nuclear Coordinate Space

Sections VA through VE present minima, saddle points, and intersections for states 1^2A, 2^2A, 3^2A, and 4^2A for the five regions of the nuclear coordinate space defined in Section IIID, and analyze the performance of $\mathbf{H}^d$ at these critical points. In all regions except for the Rydberg region, the agreement between $\mathcal{S}1$, $\mathcal{S}2$, and $\mathcal{S}3$ results – denoted respectively $\mathbf{H}^d(1)$, $\mathbf{H}^d(2)$, and $\mathbf{H}^d(3)$ - is quite good. In the Rydberg region some larger differences are found and discussed. Where possible, $\mathbf{H}^d$ predictions – points not included in the 42882 point data set –are compared with *ab initio* determinations and the results of previous work. This predictive performance is an important measure of any analytic representation.

Amplitude transfer between adjacent electronic states can be facilitated by any geometry near the seam space. Thus, a global DPEM suitable for nonadiabatic dynamics must reproduce not only the minimum energy crossing (MEX) points but also the energetically accessible points near seams of intersections. The 2^2A-3^2A and 1^2A-2^2A seams of conical intersections in the valence region play the largest role in the nonadiabatic quenching of OH. In Section VB, we present the 2^2A-3^2A and 1^2A-2^2A seams determined from $\mathbf{H}^d$ and compare with *ab initio* and previous theoretical results where possible.

A. The Entrance Channel

The entrance channel contains the asymptotic reactant structures and the van der Waals complexes on both the ground (1^2A) and excited (3^2A) state. The correct description of these structures including bond distances and harmonic frequencies is required for reliable collision dynamics, as the impact of initial conditions on nuclear dynamics cannot be overstated. Table SI3 reports the *ab initio* and $\mathbf{H}^d$ determined critical point structures and the results of previous theoretical and experimental studies where possible. Table SI4 reports vibrational and energetic information. Appendix A discusses the asymptotic entrance channel behavior of stretching the OH and HH bonds.

$\mathbf{H}^d$ reproduces the *ab initio* asymptotic OH(X) and OH(A) minima structures to within 0.001 Å. Vibrational frequencies are within 4 cm^{-1} of the *ab initio* values, and these values are in good agreement with previous results. The energy of the OH(X)+H_2 asymptotic minimum structure is -33468 (-33399) [-33428, -33428] cm^{-1}, and the energy of the A state is 0 (0) [-10, -10] cm^{-1}. The agreement between $\mathcal{S}1$, $\mathcal{S}2$, and $\mathcal{S}3$ asymptotes is an important result: if the permutationally equivalent minima at the asymptotes differed greatly, then the surface would in effect be tilted, favoring one hydrogen exchange pathway over another.

At decreased intermolecular distances, there exist T-shaped (H pointing towards the midpoint of H_2) ground state and excited state van der Waals minima. The ground state minimum occurs at an intermolecular distance (distance from O to the midpoint of HH, denoted R(OH-H_2)) of 3.279 (3.292) [3.303, 3.303] Å. This agrees reasonably well with the MRCI results

of Hoffman and Yarkony (HY)[5] (3.309 Å), but less well with the fitted CCSD(T) PES of Ma *et al*. (MKAAD)[33] (3.216 Å). The $\mathbf{H}^d$ reported intermolecular distances agree well with the calculated *ab initio* values. The D_e is 152 (231) [202, 202] cm^{-1}, lower than previous results of HY and MKAAD, which both reported 220 cm^{-1}; however, fortuitously, $\mathbf{H}^d$ overestimates the *ab initio* result. The geometric parameters of the individual moieties, OH and HH bond distances, reported by $\mathbf{H}^d$ are within 0.001 Å of the *ab initio* values of 0.966 (0.967) Å and 0.744 (0.744) Å, respectively, with the HY results presented in parentheses.

The intermolecular distance of the 3^2A state van der Waals minimum is 2.180 (2.183) [2.190, 2.190] Å and the D_e is 2793 (2774) [2759, 2759] cm^{-1}. HY reported an intermolecular distance of 2.174 Å and a D_e of 2511 cm^{-1}. The *ab initio* and $\mathbf{H}^d$ values agree for $\mathcal{S}1$ while for $\mathcal{S}2$ and $\mathcal{S}3$ minima the intermolecular distances are larger by 0.007 Å and the difference in D_e is 15 cm^{-1}. Additionally, from Table SI3 it is evident that while the *ab initio* $\mathcal{S}1$ and HY structures exhibit C_{2v} symmetry, the $\mathcal{S}2$ and $\mathcal{S}3$ minima exhibit slight C_{2v} symmetry breaking. All three $\mathcal{S}i$ (i = 1,2,3) reproduce the vibrational frequencies of the 3^2A state van der Waals minimum.

B. Valence Region

The valence region is characterized by the interaction of OH and H_2 moieties. OH and HH bond lengths are near to, or exactly at, their asymptotic values. The 3^2A adiabatic PES is attractive and barrierless from the entrance channel to 2^2A-3^2A and 1^2A-2^2A seams of conical intersections, facilitating radiationless decay of the excited OH($A^2\Sigma^+$) state. These conical intersection seams were studied extensively by Dillon and Yarkony[18] denoted DY2. The *ab initio* and $\mathbf{H}^d$ results are compared with that work.

There exist two high-symmetry 2^2A-3^2A local MEXs in the valence region: a C_{2v} MEX (Figure 3) and a $C_{\infty v}$(colinear -Figure 4) MEX. Figure 3 presents **g** and **h** vectors for the C_{2v} 2^2A-3^2A MEX. The branching space of the 2^2A-3^2A seam at the C_{2v} MEX is entirely planar. These two conical intersections are connected by a C_s seam of conical intersection, shown in Figure 5. The internal coordinate connecting the C_{2v} 2^2A-3^2A MEX with the colinear 2^2A-3^2A MEX is the $\angle OH^aH^b$ angle. Constraining this angle and optimizing the five remaining internal

N^{int} coordinates yields a curve of 2^2A-3^2A degeneracies in the nuclear coordinate space from the C_{2v} 2^2A-3^2A MEX to the colinear 2^2A-3^2A MEX. The C_{2v} MEX occurs at -10317 (-10331) [-10347, -10347] cm^{-1}, in good agreement with the DY2 reported value of -10448 cm^{-1}. The geometry of the 2^2A-3^2A C_{2v} MEX agrees well with DY2. (See Table SI5.) The largest difference is +0.005 Å in the HH distance. The colinear MEX is the lowest energy point on the 2^2A-3^2A seam. The energy of the MEX is -15471 (-15598) [-15598, -15577] cm^{-1}. The *ab initio* determined value agrees well with the DY2 reported value of -15321 cm^{-1}; however, the $\mathbf{H}^d$ determined value differs by ~120 cm^{-1}. Although $\mathbf{H}^d$ correctly reproduces the directions of vectors **g** and **h** (shown in Figure 4) and $\|\mathbf{g}\|$, it does not correctly reproduce $\|\mathbf{h}\|$. See Figure 5.

Table SI5 also reports the C_{2v} 1^2A-2^2A MEX energy which is -10689 (-10697) [-10710, -10710] cm^{-1}. It is ~370 cm^{-1} below the C_{2v} 2^2A-3^2A-MEX, and the structures are similar, excepting the intermolecular distance (shorter) and HH bond distance (longer). The agreement between $\mathbf{H}^d$ and *ab initio* determined structures is excellent. The **g** and **h** vectors for the C_{2v} 1^2A-2^2A MEX are presented in Figure 3, where the **g** vector directions are seen to be largely the same, for the 1^2A-2^2A and 2^2A-3^2A MEXs. This relation between the 1^2A-2^2A and 2^2A-3^2A MEXs is emphasized in Figure 6 which shows displacements along **g** and **h** from the 2^2A-3^2A C_{2v} MEX. The proximity of the 1^2A-2^2A seam to the 2^2A-3^2A seam and parallel g vectors facilitate transitions to the ground state from the excited 3^2A state. Upon exiting a 2^2A-3^2A conical intersection, nuclear motion is routed along the in-plane **g** and **h** vectors (see Figure 3) on the 2^2A state. As the **h** vector for the 1^2A-2^2A seam is out-of-plane, the 1^2A-2^2A seam must be entirely in-plane; and so, a wavepacket on the 3^2A state that approaches the 2^2A-3^2A seam is expected to transition to the 1^2A state via 2^2A-3^2A and 1^2A-2^2A conical intersections.

The 1^2A-2^2A crossing seam as a function of R(OH^a) distance is presented in Figure 7. The agreement between *ab initio* and $\mathbf{H}^d$ determined results is excellent.

The accurate reproduction of the out-of-plane portions of the 2^2A-3^2A seam is critical for any reliable nonadiabatic dynamics study. Figure 8 presents the 2^2A-3^2A seam as a function of an out-of-plane angle,

$$\phi = 90 - \cos^{-1}\left[\boldsymbol{R}(\mathrm{OH}^c)\cdot\left(\boldsymbol{R}(\mathrm{OH}^a)\times\boldsymbol{R}(\mathrm{OH}^b)\right)/\left(\|\boldsymbol{R}(\mathrm{OH}^c)\|\cdot\left\|\left(\boldsymbol{R}(\mathrm{OH}^a)\times\boldsymbol{R}(\mathrm{OH}^b)\right)\right\|\right)\right].$$

C. Linking Region

The linking region connects the valence region to the OH_3 Rydberg region on the $2,3^2A$ states , and the exchange,[16] region and the H_2O+H product channel on the group state PES as discussed in ref [16]. Here, there are two saddle points to consider: the 1^2A saddle point and the more challenging to describe 2^2A saddle point. The 2^2A saddle point, see Figure 9, a non-coplanar structure, exhibits a significantly stretched HH bond and directs molecular motion towards the C_{3v} Jahn-Teller region. DY1 proposed this pathway as the dominant mechanism for H_2O products. The 1^2A saddle point links reactants to the product channel on the ground state surface. See Figure 10. Table SI9 reports geometry information for the two saddle points, while Table SI10 presents the energy and vibrational frequencies.

The energy of the 2^2A saddle point is 1962 (1841) [1946, 1946] cm^{-1}, DY1 report a value of 706 cm^{-1}, and therefore accessible at experimental energies. Although DY1 results and the results presented here differ by more than 1000 cm^{-1}, the structures agree well. For this reason, the barrier height discrepancy can be addressed by shifting the A state diabat, reducing the barrier height relative to the $OH(A^2\Sigma^+)+H_2$ asymptote. A study of this shift, which has worked well in the past,[26-27] will be part of a future work including nonadiabatic dynamics. *Ab initio* and $\mathbf{H}^d$ determined vibrational modes agree well with the values reported by DY1; however, $\mathcal{S}1$ overestimates the ν_2 mode by almost 400 cm^{-1} and underestimates the imaginary mode, ν_6 by 640 cm^{-1}, while the $\mathcal{S}2$ and $\mathcal{S}3$ structures accurately reproduce the *ab initio* determined ν_2 and ν_6 frequencies. The cause of this discrepancy may be an improper scaling of the coordinate basis functions reported in the SI. The impact of these differences (fitting errors) will be assessed by starting the dynamics calculations with the initial conditions in each of $\mathcal{S}1$, $\mathcal{S}2$, and $\mathcal{S}3$.

The 1^2A saddle point has been studied extensively.[34] We compare our results, both *ab initio* and $\mathbf{H}^d$, to the single state ground state PES of Yang, Zhang, Collins, and Lee (YZCL).[35] The OH^b distance of 1.348 (1.346) [1.348, 1.346] Å is in good agreement with the distance of 1.356 Å reported by YZCL. The OH^c distance of 0.967 (0.967) [0.967, 0.967] Å and the H^aH^b

distance of 0.822 (0.823) [0.821, 0.823] Å are in excellent agreement with the YZCL values of 0.970 Å and 0.819 Å, respectively. The *ab initio* and $\mathbf{H}^d$ determined classical barrier height 2269 (2207) [2245, 2214] cm^{-1} is in reasonable accord with the result of YZCL being 2006 cm^{-1} relative to the OH(X)+ H_2 asymptote This overestimation would affect the reaction rate at a given energy, but the agreement between vibrational modes of YZCL and the results presented here should only affect the total flux up to a small, energetic shift. And, much like the 2^2A, if need be, the responsible diabat can be shifted to match the adiabatic barrier height with experimental, or in this case theoretical, values. The reasonably good reproduction of the ground state PES is a good indication of the accuracy of this DPEM.

D. Rydberg Region

The Rydberg, or exchange,[16] region of the PES is of critical importance although it constitutes a small region of nuclear coordinate space. From this region OH_3, has access to three permutationally equivalent product channels and three permutationally equivalent reactant channels. It is for this reason that symmetry-equivalent data must be included in the fit. There are several critical points in the Rydberg region that merit attention: the ground state C_{3v} minimum; the ground state D_{3h} saddle point connecting the C_{3v} minima; the Jahn-Teller crossing of states 2^2A and 3^2A; the minimum of the 4^2A state; as well as the saddle points leading to the product channel.

Table SI11 reports the geometric parameters and Table SI12 reports the energy and vibrational information for the minima and saddle points of the Rydberg region. The ground electronic state in the Rydberg region is the OH_3^+ cation with a single electron occupation of the Rydberg 3*s* orbital. The local minimum has C_{3v} symmetry and is connected by a D_{3h} saddle point to its symmetry-equivalent structure. The *ab initio* ($\mathbf{H}^d$) determined energy of the minimum is -32433 (-32468) cm^{-1} and that of the saddle point is -30670 (-30897) cm^{-1}. The agreement between the *ab initio* ($\mathbf{H}^d$) energies is satisfactory. However, the DY1 computed minimum is significantly higher at -30742 cm^{-1}. The *ab initio* and $\mathbf{H}^d$ determined PES captures approximately the C_{3v} geometry of the local minimum, as the *ab initio* ($\mathbf{H}^d$) determined OH bond distances are

found to be 1.014 (1.016), 1.014 (1.016), and 1.016 (1.015) Å; the bond lengths differ slightly from the 1.025 Å reported by DY1. The *ab initio* ($\mathbf{H}^d$) determined energies capture (capture approximately) the D_{3h} symmetry of the saddle point between C_{3v} minima, Since the distortions are small, they should have a negligible effect on dynamics. The $\mathbf{H}^d$ determined PES reproduce the *ab initio* vibrational frequencies satisfactorily with the exception of the ν_2 mode of the ground state minimum which differs from the *ab initio* results by 230 $cm^{-1.}$ All other frequencies are reproduced within 100 cm^{-1}.

The $2,3^2A$ states form a Jahn-Teller pair. Table SI13 reports geometry information for C_{3v} and D_{3h} conical intersections. In this work we are more interested in the interstate couplings also reported in Table SI13. For a more complete discussion of this Jahn-Teller system see Appendix B.

The barrier to ground state HOH+H products from the Rydberg region is 1037 (950) [956, 956] cm^{-1}, in satisfactory agreement with the DY1 value of 1210 cm^{-1}. The saddle point is non-planar. The OH^c distance is 1.213 (1.212) [1.210, 1.210] Å. DY1 report a somewhat longer bond distance of 1.225 Å. The out of plane angle is 109.52 (108.92) [109.85, 109.85]º. The OH^1/OH^2 distances are 0.985/0.985 (0.986/0.986) [0.986/0.985, 0.985/0.986] Å. Vibrational frequencies are well reproduced by $\mathbf{H}^d$. See Table SI12.

$\mathbf{H}^d$ is capable of making correct predictions. The *ab initio* ($\mathbf{H}^d$) determined C_{3v} 4^2A minimum occurs at -9179 (-9182) cm^{-1}. The OH bond distances are 0.972 (0.971), 0.971 (0.971), and 0.972 (0.971) Å, shorter than those of the C_{3v} 1^2A minimum. Vibrational frequencies are well reproduced. The agreement between the *ab initio* and $\mathbf{H}^d$ determined quantities is especially satisfying as no data for the 4^2A minimum has been included in the fitting procedure. For this critical point, the minimum was first located on the final $\mathbf{H}^d$ constructed PES, and this structure was used to begin the *ab initio* minimum search, providing an illustration of the usefulness of the analytic DPEM.

E. The Product Channel

The product channel contains the asymptotic H_2O+H structures. In this region the energies of states 2^2A, 3^2A, and 4^2A are 19804, 22976, and 36466 cm^{-1}.Consideration of the excited states in the product channel is not necessary for the reaction under study. The H_2O ground electronic state minimum has bond lengths of 0.958 (0.957) [0.957, 0.957] Å, agreeing well with experimental results. See Table SI14. The HOH angle is 104.07 (103.77) [104.20, 104.20]º, also agreeing well with established experimental results.[36] The H_2O ground state minimum is -39010 (-38989) [-39036, -39036] cm^{-1}, agreeing well with the DY1 result of -38989 cm^{-1}. Minimal differences between the product asymptotes of each set ensures equal treatment of all accessible reaction paths. Agreement between *ab initio*, $\mathbf{H}^d$, and DY1 and experimental vibration frequencies is excellent.

The *ab initio* determined reaction energy, (including zero-point energies) for $OH(X^2\Pi)$ + $H_2 \rightarrow H_2O + H$ is -4896 cm^{-1}. For reactants beginning in $\mathcal{S}1$, the $\mathbf{H}^d$ derived reaction energy (-4950) [-4957, -4957] cm^{-1} in satisfactory agreement with the experimental result of -5161 cm^{-1}.[37]

VI. Derivative Couplings and the Diabatic Representation

The least-squares procedure defines the diabatic states as a geometry-dependent rotation that minimizes the residual couplings in a least squares sense. Figure 11 shows linear synchronous transit paths from the entrance channel to the product channel. The upper panel shows *ab initio*, $\mathbf{H}^d$ adiabatic energies, and the $\mathbf{H}^d$ diabatic energies (the diagonal matrix elements and the lower panel shows the magnitude of the derivative coupling, $\mathbf{f}^{ij}$ for i,j=1,2,3. Couplings with the 4^2A state are omitted as there are no crossings relevant to the current study. The open symbols denote data points not included in the fitting data set. Three cusps are present in the lower panel of Figure 11: the first cusp is $\mathbf{f}^{23}$ at the C_{2v} 2^2A, 3^2A-MEX, the second is $\mathbf{f}^{12}$ at the C_{2v} 1^2A, 2^2A-MEX, and the third cusp is $\mathbf{f}^{23}$ at the C_{3v} 2^2A, 3^2A-MEX.

VII. Summary and Conclusions

This report presents and analyzes a four-state diabatic representation of the coupled 1, 2, 3 ^{2}A adiabatic potential energy surfaces relevant to the collisional quenching of OH($A^2\Sigma^+$) by H_2. The representation is based on high-level, multi-reference *ab initio* wavefunction data. The agreement between this *ab initio* data and the representation, $\mathbf{H}^d$, is largely very good, reporting a total RMS (MU) error of 178 (83) cm^{-1}. $\mathbf{H}^d$ is shown to accurately reproduce relevant critical points on, and conical intersections coupling among, 1, 2, 3, and 4^{2}A states. Additionally, it performs well at geometries outside of the generative data set, essential for dynamical simulations.

It is expected that the DPEM reported in this work will allow multistate quantum dynamical calculations, which will provide a greatly improved understanding of the mechanism behind the collisional quenching of OH($A^2\Sigma^+$) by H_2.

Acknowledgements: This work was supported by Department of Energy Grant (DE-SC0015997 to H.G. and D.R.Y.).

Supporting Information:

Supporting information contains the definitions of the elementary functions of **R**; the free parameters of the expansion monomials; geometric, vibrational, and energetic data for reported critical points and intersections; and corresponding geometric data and conical parameters for MEX points on 2^{2}A-3^{2}A (Figure 5 and Figure 8) and 1^{2}A-2^{2}A seams. (Figure 7). A copy of this DPEM is available in the supporting information.

Notes

The authors declare no competing financial interest.

ORCID

Christopher L. Malbon: 0000-0002-6553-7437

David R. Yarkony: 0000-0002-5446-1350

Bin Zhao: 0000-0001-5862-7402

Hua Guo: 0000-0001-9901-053X

Appendix A. Entrance Channel Asymptotic Behavior

In this appendix the non-intuitive behavior of the fit 4^2A state energy in the entrance channel as a function R(H-H) is described and explained. Figure A1 plots the 1, 2, 3, 4^2A *ab initio* and $\mathbf{H}^d$ determined adiabatic energies against R(O-H) at an intermolecular distance of 20.0 au. Here potential energy curves (PECs) look, as one would expect, like two energetically displaced doubly degenerate OH(X) PECs. The agreement between $\mathbf{H}^d$ and *ab initio* determined energies is good for short R(O-H) but deteriorates somewhat as R(O-H) becomes larger however, this occurs for energies (1) above E^{cutoff} and (2) energetically inaccessible in the low-energy collisional experiments studied here.

Figure A2 plots the *ab initio* and $\mathbf{H}^d$ determined 1, 2, 3, 4^2A adiabatic states against R(H-H) displacements at the intermolecular distance of 20.0 au. The agreement between *ab initio* and $\mathbf{H}^d$ determined energies for R(H-H)=1.0…5.0 is excellent. At small R(H-H) the 3^2A, state which corresponds to OH($A^2\Sigma^+$)+H_2(R(H-H)) is well separated from the 1^2A and 2^2A states which correspond to the OH(X) +H_2(R(H-H)) states, and the 4^2A state, which represents an excited state of OH+ H_2(R(H-H)). The shape of these PECs is not intuitive. 1, 2^2A and 3^2A states reflect the Morse form, as one expects, of the PECs as a function of R(H-H) until R(H-H) ~ 2.5 au. Here, the 4^2A state, which at this point represents excitation into the anti-bonding σ^*_{HH} orbital, has decreased significantly in energy and becomes degenerate with the 3^2A state. Differences between *ab initio* and $\mathbf{H}^d$ energies are the result of the 3^2A and 4^2A being above E^{cutoff} =5000 cm^{-1}, and once the adiabatic energies are below this fitting threshold the agreement improves significantly. At large R(H-H) there are two sets of degenerate states representing the two degenerate OH(X) states and the two degenerate ^{2}S states of H and H.[38] Both sets of degenerate

states are below E^{cutoff} and are energetically accessible from the $OH(A^2\Sigma^+)+H_2$ asymptote although there is a significant barrier.

Appendix B. The 2^2A-3^2A Jahn-Teller System

In the Rydberg region the 2^2A and 3^2A states comprise a Jahn-Teller system (See Figure B1). *Ab initio* calculations in C_1-symmetry are unable to precisely describe the *E*-state degeneracy of the C_{3v} MEX. For this reason, an optimized intersection near the C_{3v} MEX was determined for a constrained OH bond distance (1.058 Å). Two similarly constrained MEXs are generated via the hydrogen permutations, and the surface interpolates between all three intersections. This interpolated C_{3v} MEX compares well with the reported results of DY1; albeit, with slight symmetry breaking. The OH bond distance of 0.988 Å is in excellent agreement with the DY1 value of 0.987. The energy of the Jahn-Teller 2,3-MEX is -14378 cm^{-1}. This is approximately 2000 cm^{-1} below the reported values of DY1. The 2^2A-3^2A seam extends from C_{3v} to D_{3h}. A similar method of using nearby non-symmetric intersections to interpolate and describe the high-symmetry degeneracy was applied to the D_{3h} 2,3-MEX. The planar MEX is 885 cm^{-1} above the C_{3v} MEX, which compares well with DY1 value of 881 cm^{-1}. However, the OH bond distances are 0.975, 0.975, and 0.989 Å, making the structure slightly C_{2v}. This distortion is similar to that of the ground state D_{3h} saddle point discussed in Sec. VD.

A C_{3v}-symmetric Jahn-Teller system should have three minima and three saddle points equidistant from one another, forming two equilateral triangles. The $\mathbf{H}^d$ reported structures for 2^2A minima and saddle points are reported in Table SI15. Vibrational frequencies of these critical points are reported in Table SI16. Figure B2 displays the positions of the six critical points in the **g**-**h** plane with respect to the C_{3v} 2^2A-3^2A MEX point. This plot quantifies the limited symmetry breaking.

Table I. Fitting Statistics

Data Points	42882
Total symmetrized basis matrices	34729
Independent symmetrized basis matrices	33230
Total least squares coefficients	1645168
RMS Energy Error (cm^{-1})	177.57
RMS Gradient Error (%)	7.29
MU Energy Error (cm^{-1})	83.49
MU Gradient Error (%)	3.79

Table II. Root-mean-square (RMS) error and mean unsigned (MU) error for four adiabatic states of $\mathbf{H}^d$. The results reported in Ref. [22] are italicized.

State	RMS Error (cm^{-1})	MU Error (cm^{-1})
4^2A	100.50	67.26
3^2A	185.82	74.39 *621.05*
2^2A	170.55	83.18 *250.03*
1^2A	181.18	89.19 *427.47*

Figure 1. $OH + H_2$ structure with atom labeling used in this work.

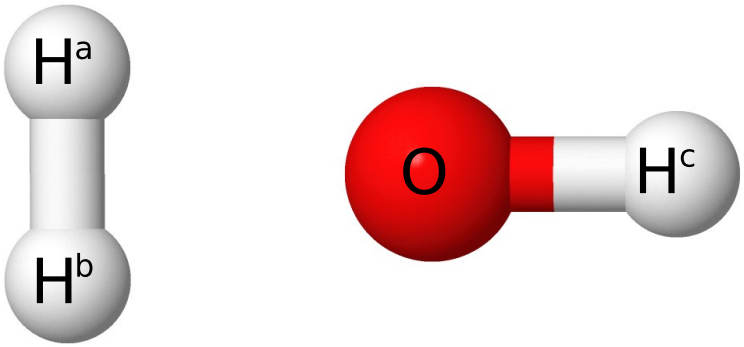

Figure 2. (a) Left ordinate: RMS (solid line) and MU (dashed) electronic energy errors in cm^{-1} for individual states as a function of electronic energy. (b) Right ordinate: density of **R** in arbitrary units.

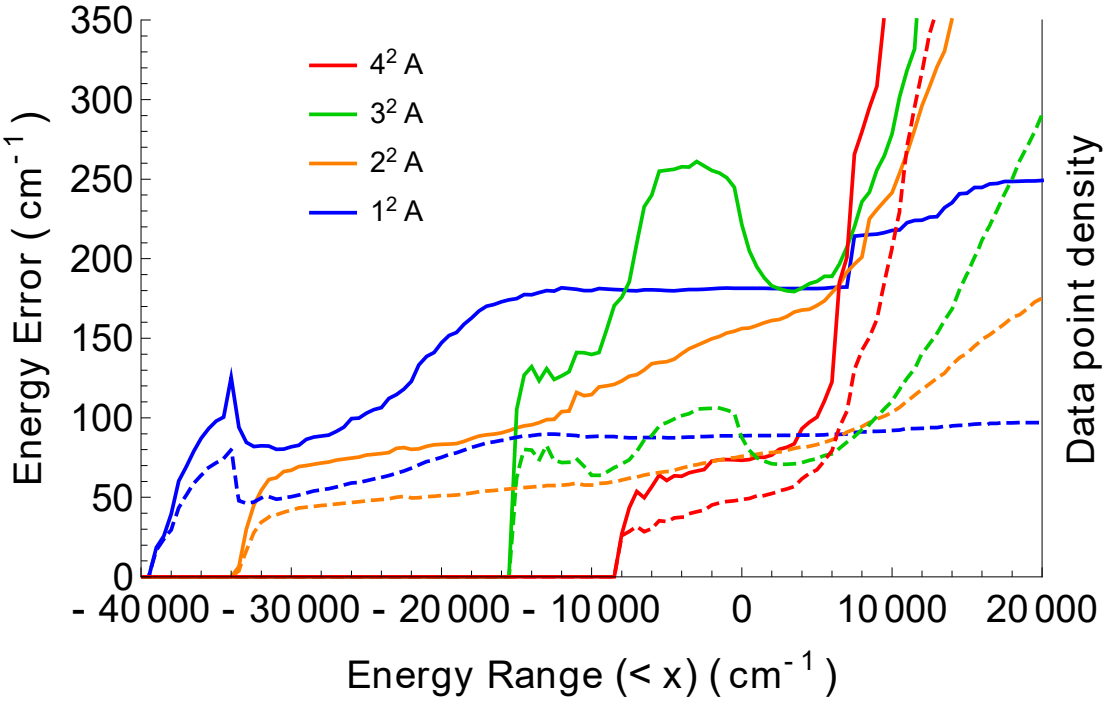

Figure 3. Mass-weighted **g** and **h** vectors for C_{2v} 2^2A-3^2A and 1^2A-2^2A MEXs in the valence region. Clockwise from top left: $\mathbf{g}^{23}$, $\mathbf{h}^{23}$, $\mathbf{h}^{12}$, $\mathbf{g}^{12}$.

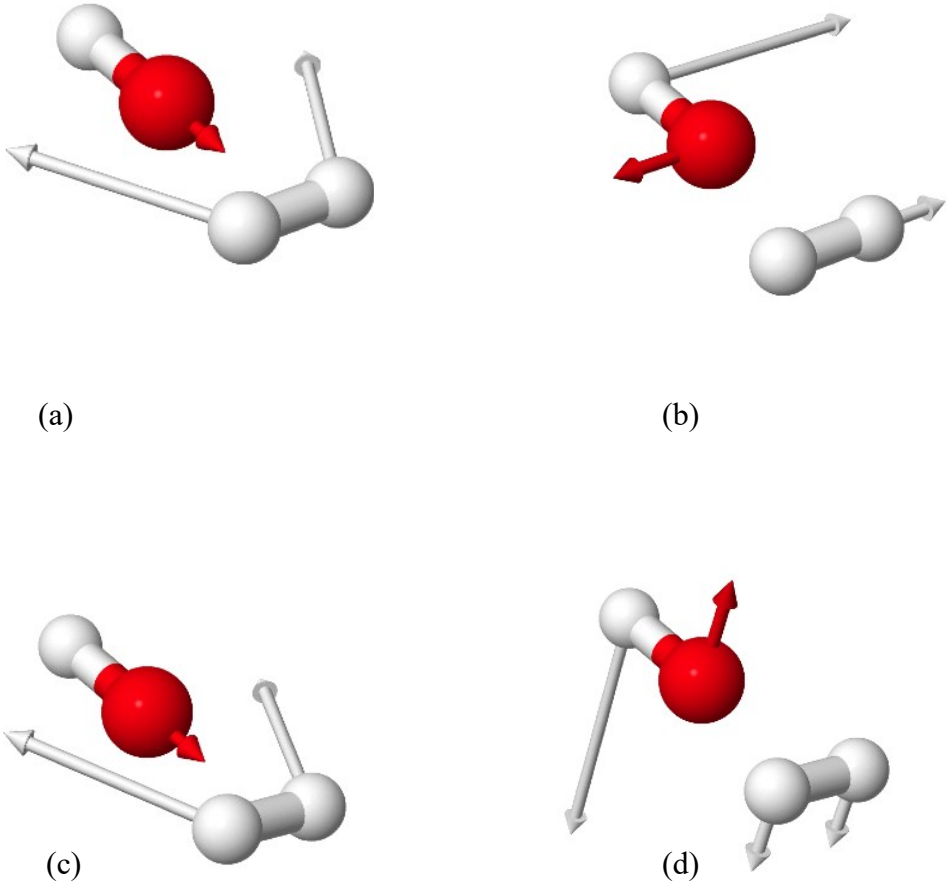

Figure 4. Mass-weighted **g** and **h** vectors for C_∞ 2^2A-3^2A MEX in the valence region. From left to right: $\mathbf{g}^{23}$, $\mathbf{h}^{23}$.

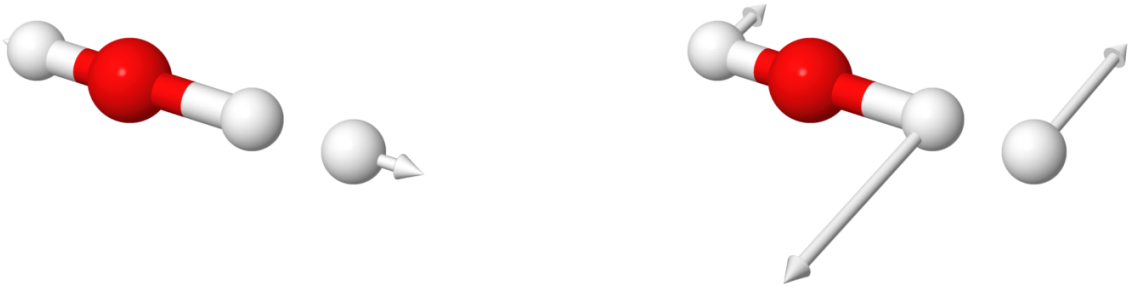

Figure 5. Plot of the 2^2A-3^2A crossing seam from the 2^2A-3^2A MEX(C_{2v}) to the colinear 2^2A-3^2A MEX. Red markers are MEX's. Solid and dashed lines are $\mathbf{H}^d$ results. Symbols are *ab initio* results.

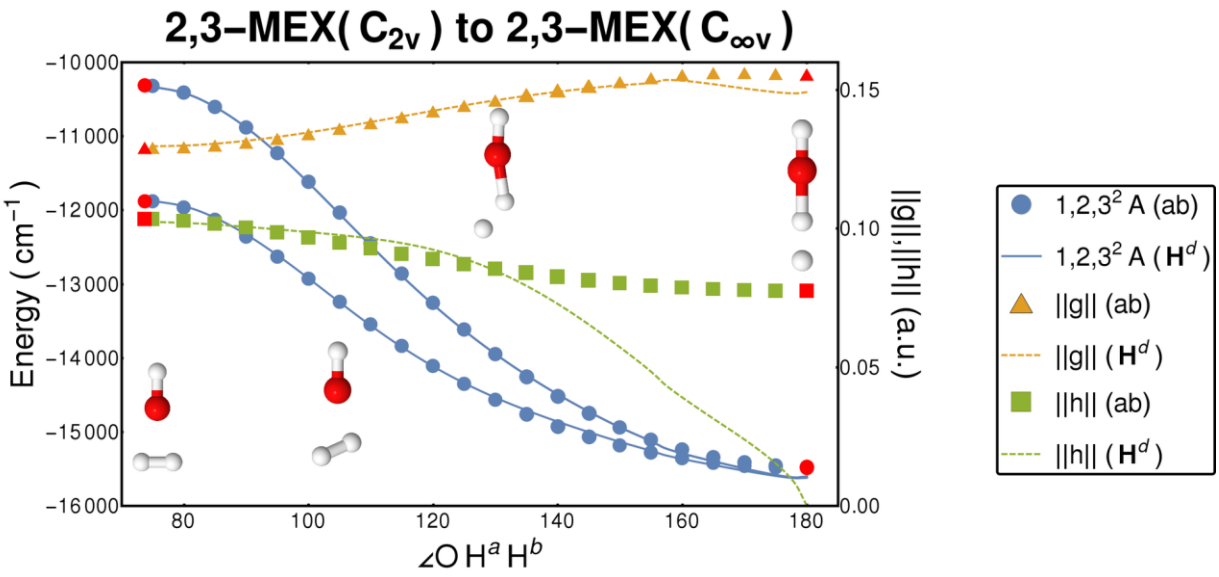

Figure 6. The 2^2A-3^2A C_{2v} MEX. x and y represent coordinates in the **g-h** plane (in atomic units), where $x = \mathbf{g}/\|\mathbf{g}\|$ and $y = \mathbf{h}/\|\mathbf{h}\|$.

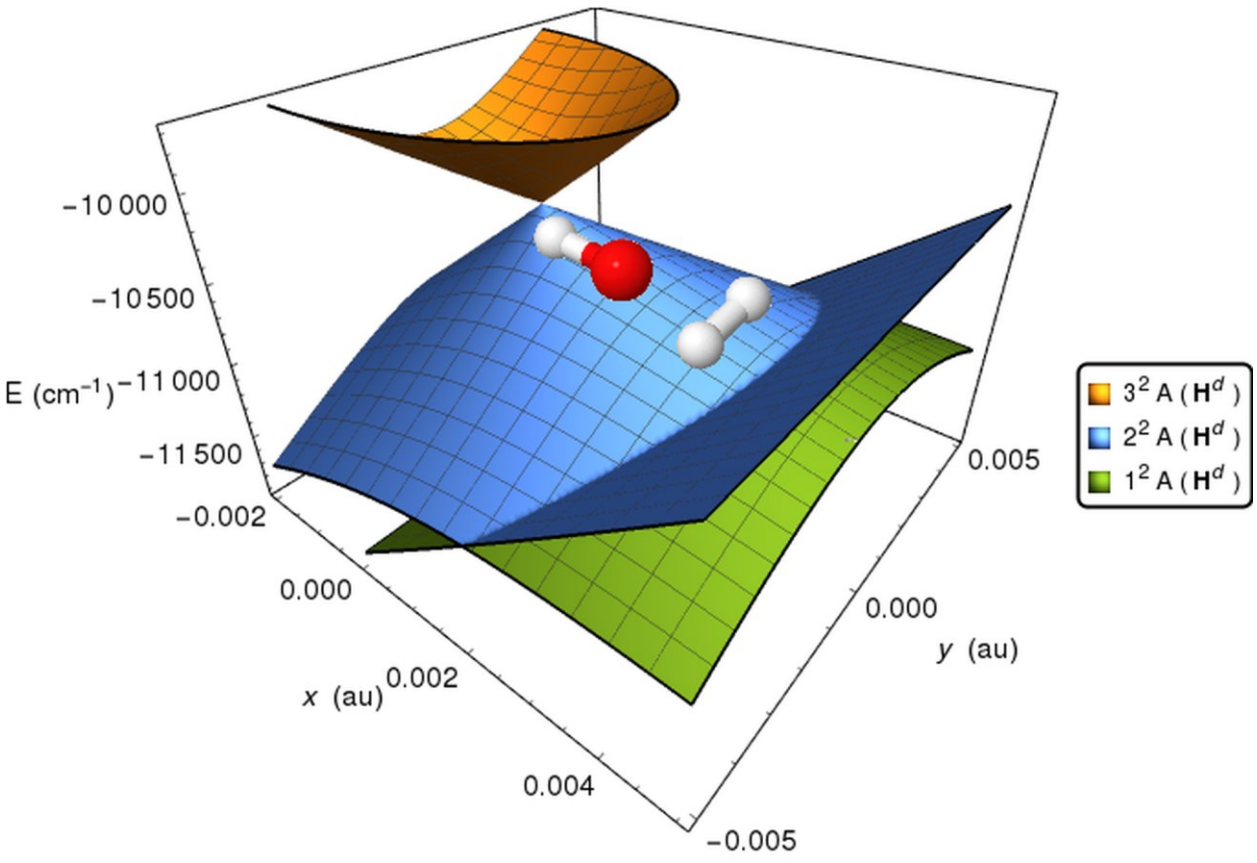

Figure 7. The 1^2A-2^2A seam at constrained $R(OH^a)$ distances. Distances are in Å.

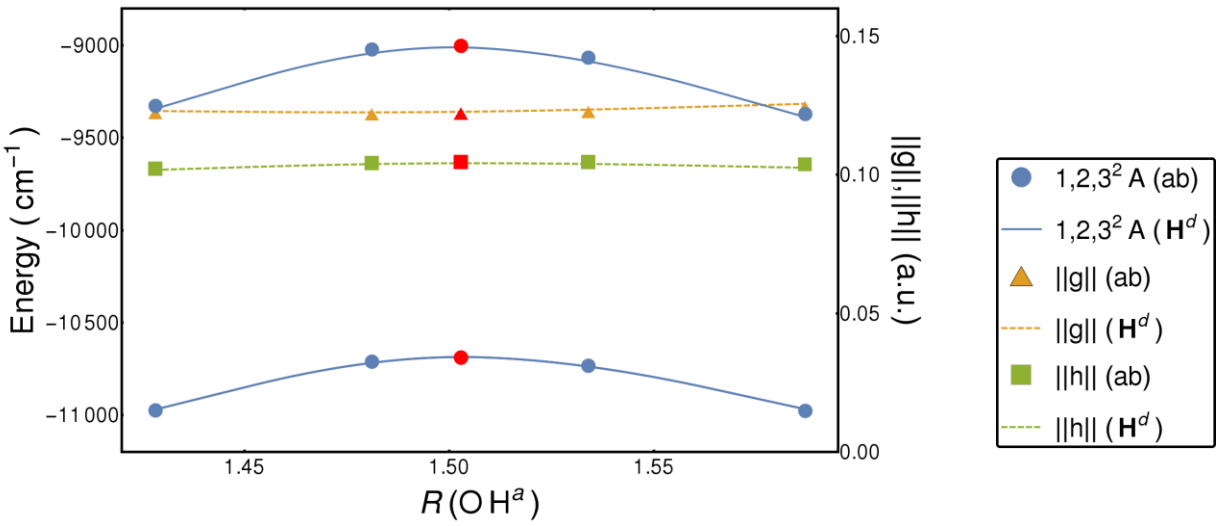

Figure 8. Plot of 2^2A-3^2A crossing seam from 2^2A-3^2A MEX (C_{2v}) along the out-of-plane angle, $\phi = 90 - \cos^{-1}\left[\boldsymbol{R}(\mathrm{OH}^c) \cdot \left(\boldsymbol{R}(\mathrm{OH}^a) \times \boldsymbol{R}(\mathrm{OH}^b)\right) / \left(\|\boldsymbol{R}(\mathrm{OH}^c)\| \cdot \left\|\left(\boldsymbol{R}(\mathrm{OH}^a) \times \boldsymbol{R}(\mathrm{OH}^b)\right)\right\|\right)\right]$, where $\boldsymbol{R}$(OX) denotes the vector from O to X. $\mathrm{OH}^{(a,b)}$ bond distances are held fixed at 2^2A-3^2A MEX (C_{2v}) values.

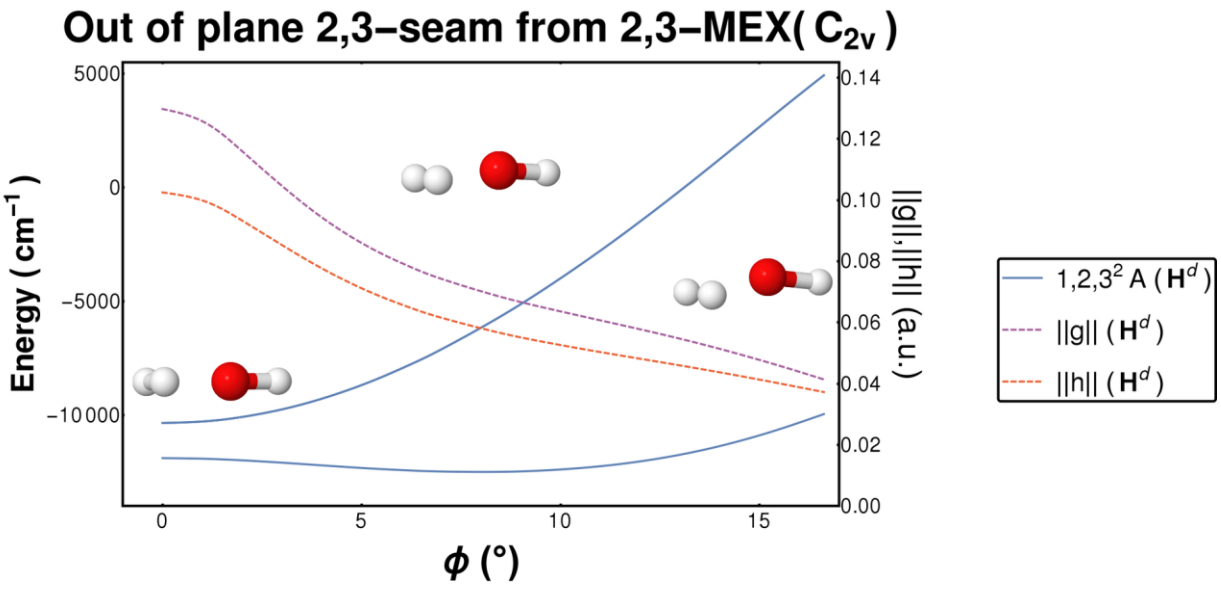

Figure 9. Reaction coordinate vector of the 2^2A linking region saddle point.

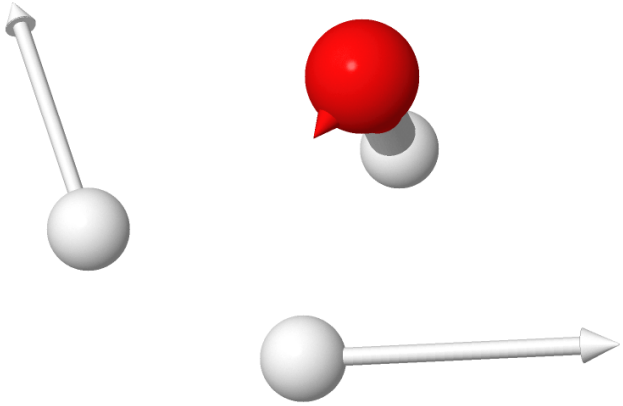

Figure 10. Reaction coordinate vector of the 1^2A linking region saddle point.

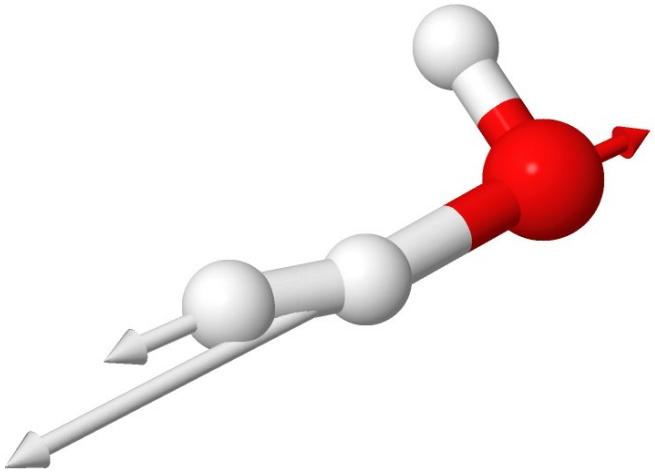

Figure 11. Cuts through the PESs from the entrance channel to the H + H_2O product channel. Circles represent *ab initio* values. Closed symbols are included in the fitting data set. Open symbols are not included in the fitting data set. Top panel: Dashed lines are $\mathbf{H}^d$ adiabatic PES. Solid lines are diagonal elements of $\mathbf{H}^d$. Black dashed line represents value of E^{cutoff}. Bottom panel: Solid lines represent $\mathbf{f}^{ij}$ of $\mathbf{H}^d$.

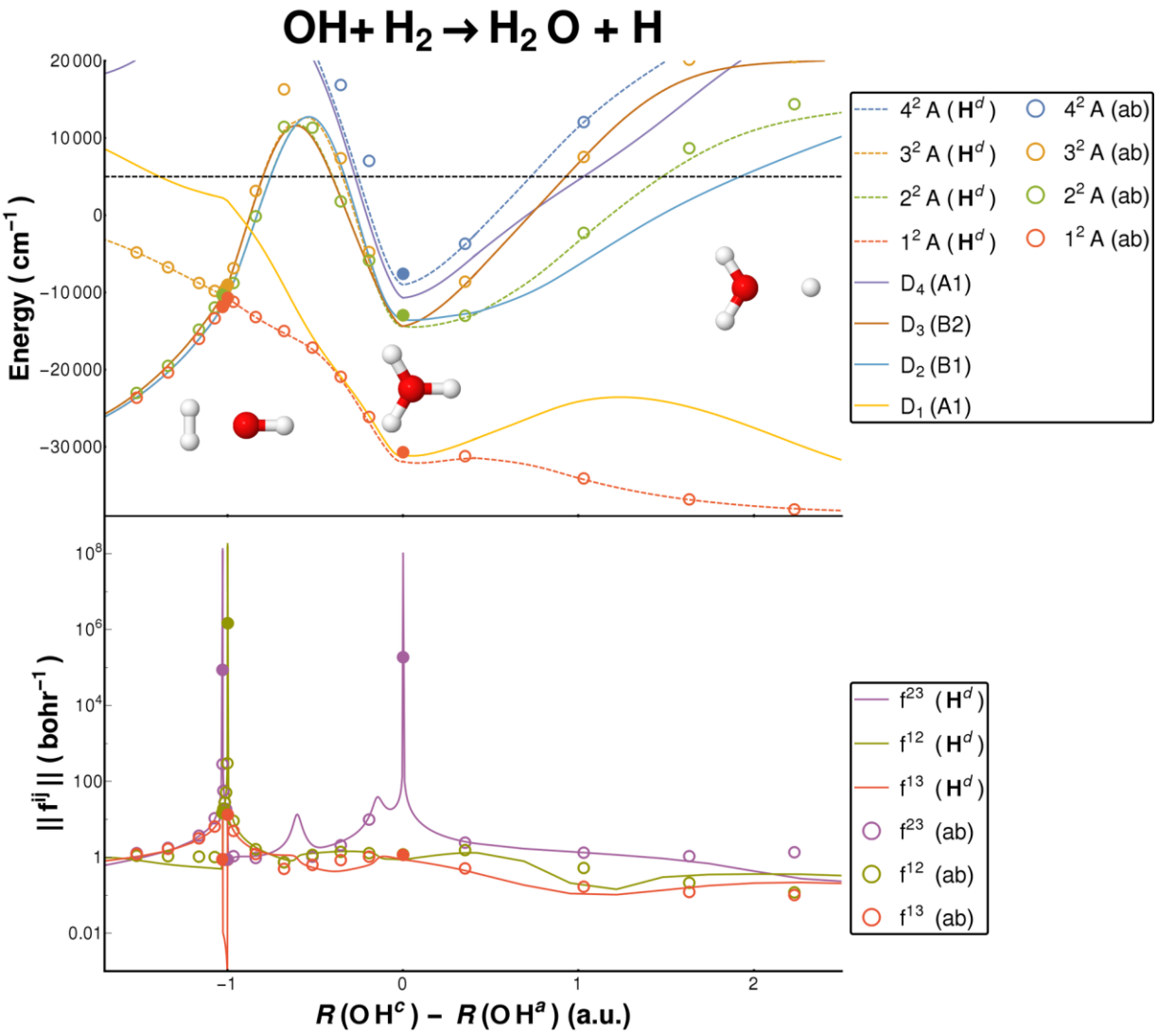

Figure A1. Plot of the 1, 2, 3, 4^2A states at entrance channel asymptote (R(O-H_2)=20 au) for the O-H dissociation.

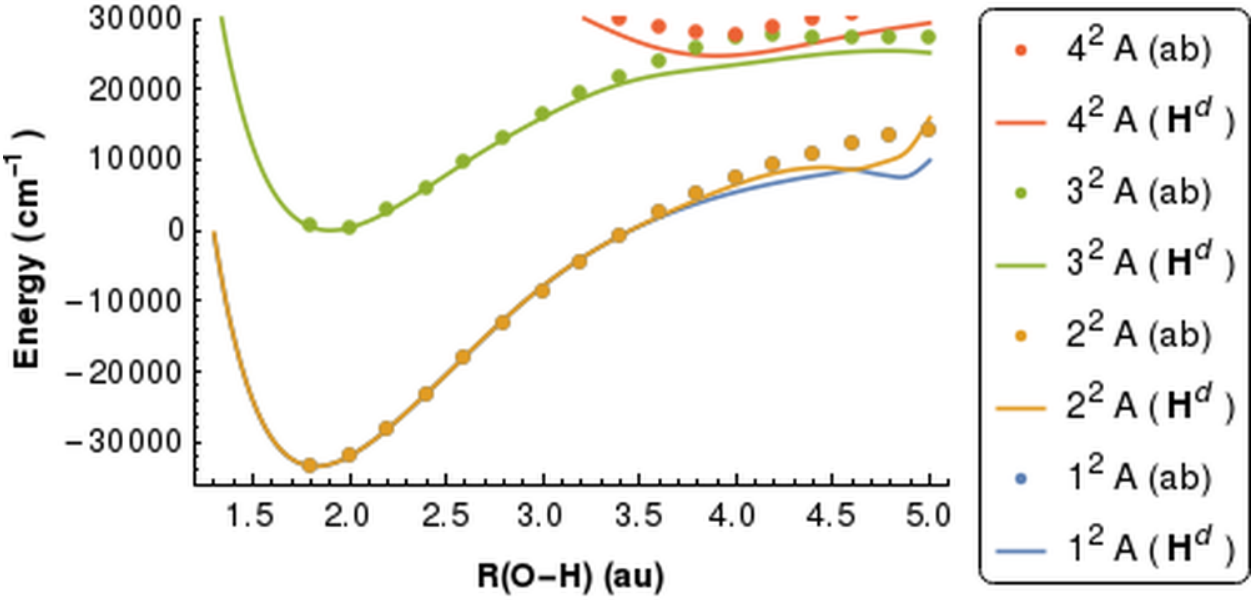

Figure A2. Plot of the 1, 2, 3, 4^2A states at entrance channel asymptote (R(O-H_2)=20 au) for the H-H dissociation.

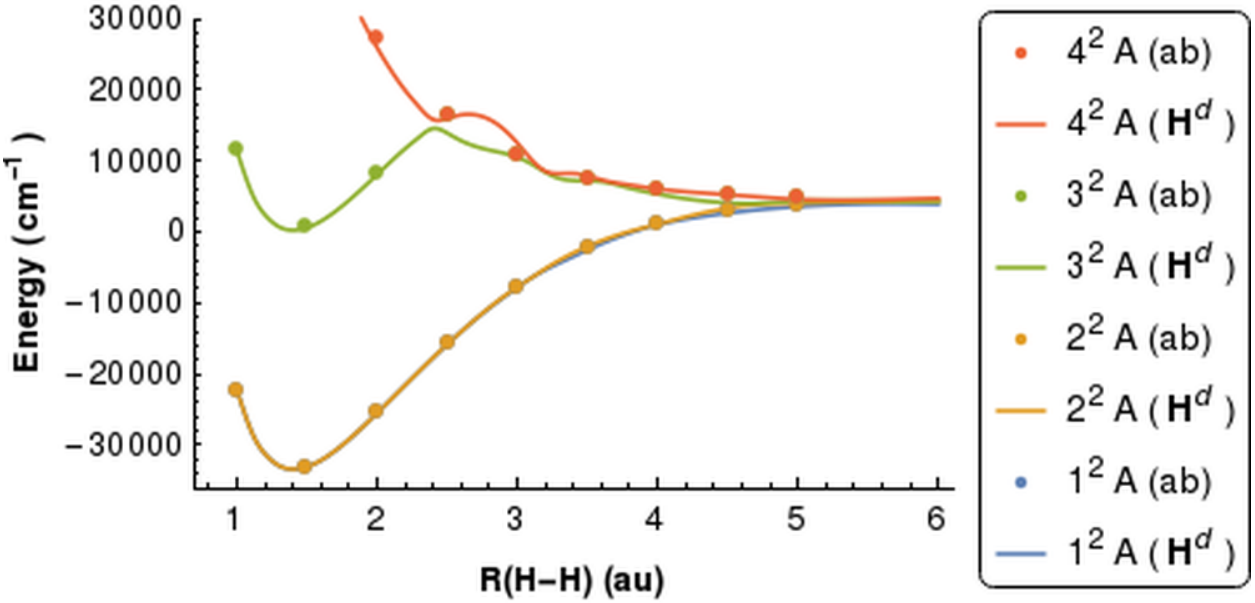

Figure B1. The 2^2A-3^2A C_{3v} MEX. Displacements are along **g** and **h**. Zero is energy of MEX, E(MEX)=-14372.8 cm^{-1}, relative to OH($A^2\Sigma^+$) + H_2 asymptote.

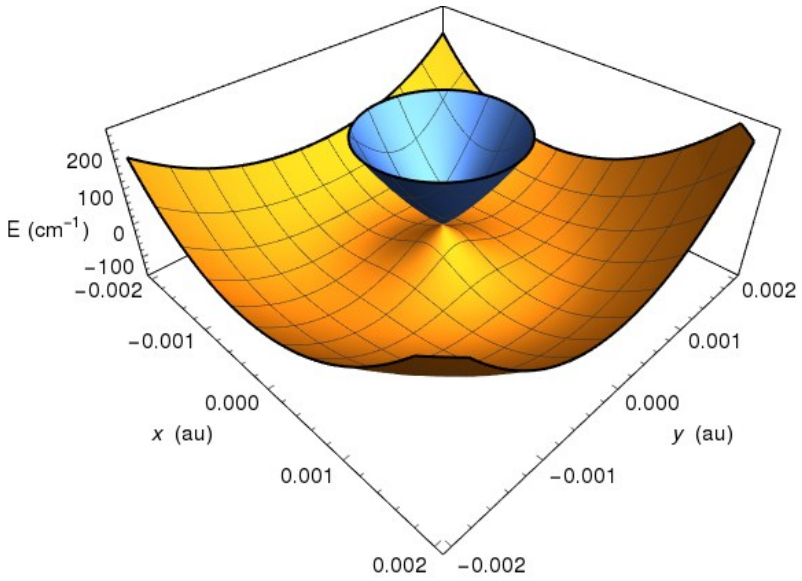

Figure B2. The **g-h** plane of 2^2A-3^2A C_{3v} MEX. Black double-cone represents MEX. Blue symbols represent minima, and orange symbols represent saddle points. Angles of triangle formed by blue symbols (minima): 67.80, 56.10º, 56.10 º. Angles of triangle formed by orange symbols (saddle points): 40.47º, 69.47º, 70.03º.

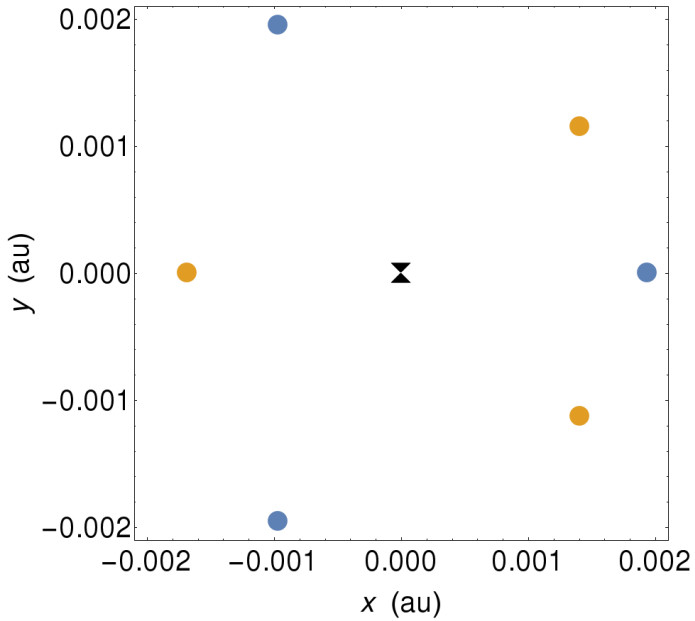

References

1. Warnatz, J.; Maas, U.; Dibble, R. W., *Combustion : Physical and Chemical Fundamentals, Modelling and Simulation, Experiments, Pollutant Formation*. Springer: 1996.
2. Wayne, R. P., *Chemistry of Atmospheres*. Oxford University Press: Oxford, 2000.
3. Graedel, T. E.; Crutzen, P. J., *Atmospheric Change: An Earth System Perspective*. W. H. Freeman and Company: New York, 1993.
4. Yarkony, D. R., Substituent effects and the noncrossing rule: The importance of reduced symmetry subspaces. I. The quenching of OH(A 2Σ+) by H2. *The Journal of Chemical Physics* **1999,** *111* (15), 6661-6664.
5. Hoffman, B. C.; Yarkony, D. R., The role of conical intersections in the nonadiabatic quenching of OH($A^2\Sigma^+$) by molecular hydrogen. *J. Chem. Phys.* **2000,** *113*, 10091-10099.
6. Dempsey, L. P.; Murray, C.; Lester, M. I., Product branching between reactive and nonreactive pathways in the collisional quenching of OH $A^2\Sigma^+$ radicals by H_2. *J. Chem. Phys.* **2007,** *127*, 151101.
7. Lehman, J. H.; Dempsey, L. P.; Lester, M. I.; Fu, B.; Kamarchik, E.; Bowman, J. M., Collisional quenching of OD $A^2\Sigma^+$ by H_2: Experimental and theoretical studies of the state-resolved OD $X^2\Pi$ product distribution and branching fraction. *J. Chem. Phys.* **2010,** *133*, 164307.
8. Anderson, D. T.; Todd, M. W.; Lester, M. I., Reactive quenching of electronically excited OH radicals in collisions with molecular hydrogen. *J. Chem. Phys.* **1999,** *110*, 11117-11120.
9. Todd, M. W.; Anderson, D. T.; Lester, M. I., Reactive quenching of OH A $^2\Sigma^+$ in collisions with molecular deuterium via nonadiabatic passage through a conical intersection. *J. Phys. Chem. A* **2001,** *105*, 10031-10036.
10. Lehman, J. H.; Bertrand, J. L.; Stephenson, T. A.; Lester, M. I., Reactive quenching of OD $A^2\Sigma^+$ by H_2: Translational energy distributions for H- and D-atom product channels. *J. Chem. Phys.* **2011,** *135*, 144303.
11. Ortiz-Suárez, M.; Witinski, M. F.; Davis, H. F., Reactive quenching of OH($A^2\Sigma^+$) by D_2 studied using crossed molecular beams. *J. Chem. Phys.* **2006,** *124* (20), 201106.
12. Cleary, P. A.; Dempsey, L. P.; Murray, C.; Lester, M. I.; Kłos, J.; Alexander, M. H., Electronic quenching of OH $A^2\Sigma^+$ radicals in single collision events with molecular hydrogen: Quantum state distribution of the OH $X^2\Pi$ products. *J. Chem. Phys.* **2007,** *126*, 204316.
13. Kamarchik, E.; Fu, B.; Bowman, J. M., Communications: Classical trajectory study of the postquenching dynamics of OH A^2S^+ by H_2 initiated at conical intersections. *J. Chem. Phys.* **2010,** *132*, 091102.
14. Fu, B.; Kamarchik, E.; Bowman, J. M., Quasiclassical trajectory study of the postquenching dynamics of OH A^2S^+ by H_2/D_2 on a global potential energy surface. *J. Chem. Phys.* **2010,** *133*, 164306.
15. Zhang, P.-Y.; Lu, R.-F.; Chu, T.-S.; Han, K.-L., Quenching of OH($A^2\Sigma^+$) by H_2 through conical intersections: Highly excited products in nonreactive channel. *J. Phys. Chem. A* **2010,** *114*, 6565-6568.
16. Collins, M. A.; Godsi, O.; Liu, S.; Zhang, D. H., An ab initio quasi-diabatic potential energy matrix for OH($^2\Sigma$) + H_2. *J. Chem. Phys.* **2011,** *135*, 234307.

17. Godsi, O.; Evenhuis, C. R.; Collins, M. A., Interpolation of multidimensional diabatic potential energy matrices. *J. Chem. Phys.* **2006,** *125* (10), 104105.
18. Dillon, J.; Yarkony, D. R., Seams of conical intersections relevant to the quenching of OH($A^2\Sigma^+$) by collisions with H_2. *J. Phys. Chem. A* **2013,** *117* (32), 7344-7355.
19. Dillon, J.; Yarkony, D. R., On the mechanism for the nonadiabatic reactive quenching of OH($A^2\Sigma^+$) by $H_2(^1\Sigma_g^+)$: The role of the 2^2A state. *J. Chem. Phys.* **2013,** *139* (6), 064314.
20. Guo, H.; Yarkony, D. R., Accurate nonadiabatic dynamics. *Phys. Chem. Chem. Phys.* **2016,** *18*, 26335-26352.
21. Zhang, D. H.; Guo, H., Recent advances in quantum dynamics of bimolecular reactions. *Annu. Rev. Phys. Chem.* **2016,** *67*, 135-158.
22. Shu, Y.; Kryven, J.; Oliveira-Filho, A. G. S. d.; Zhang, L.; Song, G.-L.; Li, S. L.; Meana-Pañeda, R.; Fu, B.; Bowman, J. M.; Truhlar, D. G., Direct diabatization and analytic representation of coupled potential energy surfaces and couplings for the reactive quenching of the excited 2Σ+ state of OH by molecular hydrogen. *The Journal of Chemical Physics* **2019,** *151* (10), 104311.
23. Zhu, X.; Yarkony, D. R., Fitting coupled potential energy surfaces for large systems: Method and construction of a 3-state representation for phenol photodissociation in the full 33 internal degrees of freedom using multireference configuration interaction determined data. *J. Chem. Phys.* **2014,** *140*, 024112
24. Zhu, X.; Yarkony, D. R., On the representation of coupled adiabatic potential energy surfaces using quasi-diabatic Hamiltonians: A distributed origins expansion approach. *J. Chem. Phys.* **2012,** *136*, 174110.
25. Zhu, X.; Yarkony, D. R., Quasi-diabatic representations of adiabatic potential energy surfaces coupled by conical intersections including bond breaking: A more general construction procedure and an analysis of the diabatic representation. *J. Chem. Phys.* **2012,** *137*, 22A511.
26. Zhu, X.; Malbon, C. L.; Yarkony, D. R., An improved quasi-diabatic representation of the 1, 2, 3^1A coupled adiabatic potential energy surfaces of phenol in the full 33 internal coordinates. *J. Chem. Phys.* **2016,** *144* (12), 124312.
27. Malbon, C. L.; Yarkony, D. R., Multistate, multichannel coupled diabatic state representations of adiabatic states coupled by conical intersections. CH_2OH photodissociation. *J. Chem. Phys.* **2017,** *146* (13), 134302.
28. Lischka, H.; Müller, T.; Szalay, P. G.; Shavitt, I.; Pitzer, R. M.; Shepard, R., Columbus—a program system for advanced multireference theory calculations. *WIRS: Comput. Mol. Sci.* **2011,** *1* (2), 191-199.
29. Longuet-Higgins, H. C., The symmetry groups of non-rigid molecules. *Mol. Phys.* **1963,** *6*, 445-460.
30. Chen, J.; Xu, X.; Xu, X.; Zhang, D. H., A global potential energy surface for the H_2 + OH ↔ H_2O + H reaction using neural networks. *J. Chem. Phys.* **2013,** *138* (15), 154301.
31. Li, Z. H.; Ahren W. Jasper; David A. Bonhommeau; Valero, R.; Truhlar, D. G. *ANT 2009*, University of Minnesota: Minneapolis, 2009.
32. Tully, J. C., Molecular dynamics with electronic transitions. *J. Chem. Phys.* **1990,** *93*, 1061-1071.

33. Ma, Q.; Kłos, J.; Alexander, M. H.; Avoird, A. v. d.; Dagdigian, P. J., The interaction of OH(X2Π) with H2: Ab initio potential energy surfaces and bound states. *The Journal of Chemical Physics* **2014,** *141* (17), 174309.
34. Zhang, D. H.; Zhang, J. Z. H.; Zhang, Y.; Wang, D.; Zhang, Q., Quantum dynamics study of the reaction HD + OH -> H + DOH, D + HOH. *J. Chem. Phys.* **1995,** *102*, 7400.
35. Yang, M.; Zhang, D. H.; Collins, M. A.; Lee, S.-Y., Ab initio potential-energy surface for the reactions OH + H_2 → H_2O + H. *J. Chem. Phys.* **2001,** *115*, 174-178.
36. Herzberg, G., *Molecular Spectra and Molecular Structure, Vol. 3, Electronic Spectra of Polyatomic Molecules*. Van Nostrand: Princeton, 1966.
37. Huber, K. P.; Herzberg, G., *Molecular Spectra and Molecular Structure, IV, Constants of Diatomic Molecules*. van Norstrand: Princeton, 1979.
38. Sharp, T. E., Potential-energy curves for molecular hydrogen and its ions. In *Atomic Data and Nuclear Data Tables*, 1971; Vol. 2, p 119.
39. Herzberg, G., *Molecular Spectra and Molecular Structure, Vol. 2, Infrared and Raman Spectra of Polyatomic Molecules*. Van Nostrand: Princeton, 1945.

TOC

1^2A, 2^2A, and 3^2A electronic states of OH(A)+H_2 where conical intersections facilitate the quenching of OH(A) by H_2.